Research Square

Preprints are preliminary reports that have not undergone peer review.
They should not be considered conclusive, used to inform clinical practice,
or referenced by the media as validated information.

Sequential template-mediated synthesis of interstitially boron-incorporated intermetallic Pt-M nanosheets

Jong Wook Hong

jwhong@kentech.ac.kr

Korea Institute of Energy Technology https://orcid.org/0000-0003-2617-2612

Hafidatul Wahidah

University of Ulsan https://orcid.org/0009-0003-1731-9907

Hwang Hyun Wook

Ajou University

Bae Jin-Gyu

Kyungpook National University

Ghufran Azizar

Korea Institute of Energy Technology

Kyeong Hoon Moon

Korea Institute of Energy Technology

Whang Youngjoo

Korea Institute of Energy Research https://orcid.org/0009-0004-4583-1374

Ji Hoon Lee

Kyungpook National University

Seok Ki K im

Ajou University

Article

Keywords:

Posted Date: August 24th, 2026

DOI: https://doi.org/10.21203/rs.3.rs-10673128/v1

License: This work is licensed under a Creative Commons Attribution 4.0 International License.
Read Full License

Additional Declarations: There is **NO** Competing Interest.

Abstract

Integrating interstitial light elements into ordered intermetallic frameworks within ultrathin two-dimensional (2D) nanostructures presents a fundamental synthetic conflict. Intermetallic ordering requires high-temperature annealing that sinters ultrathin nanosheets (NSs), whereas premature metal–nonmetal bonding suppresses the disorder-to-order transition. Here we overcome this incompatibility through a sequential template-mediated strategy. A thickness-controlled SiO_2 layer affords $L1_0$-ordered PtNi NSs without morphological degradation, and the high atomic-diffusion barrier of the ordered superlattice then permits interstitial boron incorporation while preserving both the ordering and the ultrathin geometry. The resulting Int-PtNi-B NSs deliver mass activity of 4.99 A mg^{-1}_{Pt} and specific activity of 12.25 mA cm^{-2} for oxygen reduction reaction (ORR), with only 22.8% activity loss after 100,000 cycles. Extension to Int-PtCo-B, Int-PtFe-B, and Int-PtMn-B NSs establishes compositional generality. *In-situ* X-ray absorption spectroscopy and density functional theory show that ordering suppresses surface oxidation and restructuring, while a boron-induced ligand effect optimizes oxygen-intermediate binding.

Introduction

Multifunctionality at the nanoscale requires rational design of nanostructures combining components with dissimilar physicochemical characteristics[1–6]. Among various strategies, a promising route integrates metal–nonmetal interstitial alloys with high-surface-area architectures, such as ultrathin two-dimensional (2D) nanosheets (NSs)[7–11]. This enables atomic-level control of metal–nonmetal interactions while retaining abundant active sites[12–16]. Interstitial nonmetal atoms induce strong d-sp orbital hybridization, providing a lever for tuning the d-band center and adsorption energetics[17–26]. However, synthesizing such interstitial alloy NSs is challenging, as metal–nonmetal alloying often causes undesirable structural deformation[27–31]. Moreover, loss of interstitial elements during catalysis can destabilize the host lattice and diminish the catalytic benefits of interstitial incorporation[32–36].

Intermetallics with long-range atomic ordering have attracted attention as a platform for enhancing both catalytic activity and structural stability[37–44]. Unlike random alloys, which degrade compositionally and morphologically during catalysis, intermetallics with periodic heterogeneous metal–metal bonds offer superior thermodynamic stability[45–58]. Motivated by these findings, integrating ordered intermetallic metal–metal bonding with precisely engineered metal–nonmetal interstitial interactions in ultrathin 2D NSs represents a promising strategy for next-generation catalysts that simultaneously achieve high activity and durability. However, realizing such complex architectures poses significant synthetic challenges. Intermetallic phase formation typically requires high-temperature annealing, which often leads to nanostructure sintering and loss of controlled morphology[59–67]. Moreover, achieving atomic-level control over both metal–nonmetal interstitial bonding and ordered metal–metal arrangements within ultrathin 2D architectures remains a significant hurdle.

Here, we report a rational synthetic approach to interstitially boron-incorporated intermetallic PtNi alloy NSs (Int-PtNi-B NSs), characterized by ordered Pt–Ni atomic arrangements and tunable Pt/Ni–B interactions. A SiO_2 passivation layer of controlled thickness simultaneously prevents NS sintering and facilitates the disorder-to-order transition during annealing. The robust Pt–Ni intermetallic bonds then establish a high atomic diffusion barrier that preserves both the ordered arrangement and the 2D morphology during subsequent B-incorporation, and the strategy extends to Int-PtM-B NSs (M = Co, Fe, and Mn). We then systematically varied the metal-to-B atomic ratio (Pt and Ni to B) and investigated the ligand and strain effects on the oxygen reduction reaction (ORR). Int-PtNi-B NSs containing 14.3% B exhibited exceptional performance, achieving a mass activity of 4.99 A mg^{-1}_{Pt} and a specific activity of 12.25 mA cm^{-2}. Notably, the catalyst demonstrated outstanding durability, with only 22.8% activity loss after 100,000 potential cycles in acidic electrolyte. This simultaneous enhancement of activity and durability is attributed to modulation of the electronic structure at metal sites via synergistic effects of interstitial B-incorporation and intermetallic Pt–Ni ordering, and formation of robust Pt–Ni interactions that suppress surface atomic rearrangement and chemical degradation.

Results and discussion

Synthesis and characterization of Int-PtNi-B NSs

The synthesis of Int-PtNi-B NSs, with an ordered Pt–Ni atomic arrangement and controlled B-incorporation into interstitial lattice sites, was achieved via a sequential template-mediated approach (Fig. 1a). Porous disordered PtNi NSs were prepared by thermally diffusing Ni into pre-synthesized porous Pt NSs (Fig. 1b and Supplementary Figs. 1 and 2), followed by deposition of a conformal SiO_2 layer (15 nm) to yield PtNi@SiO_2 NSs (Supplementary Fig. 3). Annealing PtNi@SiO_2 NSs at 600°C under an H_2/Ar for 6 h induces intermetallic ordering (Fig. 1c and Supplementary Fig. 4), and removal of the SiO_2 shell yields porous Int-PtNi NSs (Fig. 1d and Supplementary Fig. 5). Finally, B atoms are interstitially incorporated under controlled reaction-atmosphere conditions, affording Int-PtNi-B NSs of average thickness 3.64 ± 0.47 nm (Fig. 1e and Supplementary Fig. 6). Atomic resolution high-angle annular dark-field scanning transmission electron microscopy (HAADF-STEM) images and Z-contrast profiles confirm long-range $L1_0$ ordering (Fig. 1f–i). HAADF-STEM-energy-dispersive X-ray spectroscopy (EDS) elemental mapping (Fig. 1j,k) and line-profile analyses (Fig. 1l) confirm uniform B-incorporation with structural integrity retained. The Pt/Ni/B atomic ratio of Int-PtNi-B NSs determined by inductively coupled plasma–optical emission spectroscopy (ICP-OES) is 45.5:40.2:14.3, matching the Pt/Ni ratio of 1:1 in the PtNi random alloy NSs. X-ray diffraction (XRD) patterns corroborate the atomic ordering changes observed by TEM. The pattern in Fig. 1m shows the structural transition of disordered PtNi NSs with an fcc crystal structure to an intermetallic phase with an fct crystal structure upon annealing. Following B-incorporation, Int-PtNi-B NSs exhibit lattice expansion while maintaining the $L1_0$-type intermetallic phase, as evidenced by diffraction peak shifts to lower angles compared with Int-PtNi NSs, further confirming interstitial B-incorporation into the PtNi intermetallic lattice. Rietveld refinement, in combination with

extended X-ray absorption fine structure (EXAFS) analysis, provides deeper structural insight into the ordering transition and B insertion, indicating that B atoms preferentially occupy octahedral sites coordinated by four Ni and two Pt atoms (Supplementary Fig. 7 and Supplementary Table 1). Furthermore, the intermetallic phase displays noticeable contraction along the c-axis lattice parameter compared with its disordered PtNi counterpart, whereas interstitial B-incorporation markedly expands the a- and b-axis lattice parameters (Supplementary Fig. 8 and Supplementary Table 1). These crystallographic observations are consistent with local structure evolution of Pt and Ni atoms, as corroborated by Pt L_3-edge and Ni K-edge EXAFS analyses (Fig. 1n,o, Supplementary Figs. 9, 10 and Supplementary Tables 2–6). Notably, thermal treatment to form the intermetallic phase effectively eliminated discernible surface oxide contributions (*i.e.*, Pt–O and Ni–O paths), while strengthening intermetallic Pt–Ni interactions. The Pt–Ni (equivalently, Ni–Pt) bond distance slightly contracted from 2.620 to 2.607 Å upon thermal treatment, consistent with the XRD peak shift toward higher angles (Fig. 1m). Concurrently, EXAFS fitting confirms increased heterometallic coordination after intermetallic ordering (Supplementary Tables 4–6). Following B-incorporation, Int-PtNi-B NSs display an elongated Pt–Ni bond distance (2.607 Å → 2.623 Å), consistent with the lattice expansion evidenced by XRD (Fig. 1m).

X-ray absorption near-edge structure (XANES) analysis was employed to investigate the effects of phase transition and B incorporation on the electronic structures and local environments of Pt and Ni (Supplementary Fig. 11). For both the Pt L_3- and Ni K-edge spectra, the intermetallic samples exhibit lower white-line intensities compared to those of disordered PtNi NSs, indicative of fewer unoccupied *d*-band states due to enhanced electron sharing between Pt and Ni atoms in the ordered structure[68–71]. Furthermore, X-ray photoelectron spectroscopy (XPS) was employed to compare the electronic structures of the synthesized samples. The Pt 4f spectra shows that the majority of near-surface Pt of the NSs is in the metallic state (Supplementary Fig. 12a). Meanwhile, the Ni 2p XPS spectra reveal that after the phase transition and B-incorporation, the percentage of near-surface Ni(II) in Int-PtNi-B NSs decreases compared to that of disordered PtNi NSs and Int-PtNi NSs (Supplementary Fig. 12b), indicating that B insertion enhances the metallic character of Ni through the formation of Ni–B bonds, thereby elucidating the role of B in modulating the surface electronic structure of the catalyst. This is further supported by the XPS valence band spectra (Supplementary Fig. 13), in which a downshift in the *d*-band center is observed for Int-PtNi-B NSs, reflecting the unique electronic structure induced by the synergistic effects of intermetallic ordering and B incorporation.

Establishing ordered Pt–Ni bonds prior to B-incorporation is critical for the synthesis of Int-PtNi-B NSs (Fig. 2a). Because periodic Pt–Ni bonding is enthalpically more stable than its disordered counterpart, the pre-formed ordered lattice imposes a high atomic diffusion barrier that suppresses Pt and Ni migration during B-incorporation, thereby preserving the ordered arrangement, as verified by XRD (Fig. 2b,c). In contrast, introducing B prior to annealing fails to drive the disorder-to-order transition under otherwise identical conditions (Fig. 2b,c). This is attributed to the strong Pt–B and Ni–B interactions formed at the early synthetic stage, which restrict thermal migration of Pt and Ni atoms. In addition, both

the presence and thickness of the SiO_2 protective layer are crucial for achieving a highly ordered intermetallics while preserving the ultrathin 2D morphology. Thermal annealing of disordered PtNi NSs without SiO_2 layer, or with thin SiO_2 coatings (5 and 10 nm), leads to severe morphological deformation (Supplementary Fig. 14). Consistently, XRD patterns of these samples exhibit markedly weaker superlattice (110) peaks and a correspondingly low degree of ordering (Fig. 2d,g), confirming that the SiO_2 coating not only preserves the 2D morphology but also facilitates the disorder-to-order transition. Beyond the sequential strategy and SiO_2 shell thickness, the annealing temperature and time are key parameters for maximizing ordering while retaining the ultrathin 2D morphology (Fig. 2e-i). Systematic optimization of these parameters reveals that annealing PtNi@SiO_2 NSs at 600°C for 6 h produces Int-PtNi NSs with a high degree of intermetallic ordering. The sequential template-mediated strategy is extended to other Int-PtM-B NSs (M = Co, Fe, and Mn), which retain their 2D morphology with homogeneous elemental distributions, comparable B contents, and the superlattice reflections of the ordered intermetallic phase, demonstrating the compositional versatility of this synthetic approach (Supplementary Fig. 15).

Electrochemical ORR performance of catalysts

Cyclic voltammograms (CVs) and geometric-area-normalized linear sweep voltammetry (LSV) curves of the prepared catalysts were measured in 0.1 M $HClO_4$ to (Supplementary Fig. 16a,b). Int-PtNi-B NSs exhibit a half-wave potential ($E_{1/2}$) of 978 mV, substantially more positive than different catalysts (Fig. 3a and Supplementary Fig. 16b). Among the catalysts, Int-PtNi-B NSs deliver the highest ORR activity, with a mass activity of 4.99 A mg^{-1}_{Pt} and specific activity of 12.25 mA cm^{-2} at 0.9 V_{RHE}, corresponding to 21.7- and 28.5-fold improvements over Pt/C, respectively (Fig. 3b and Supplementary Fig. 17). Both mass and specific activities of Int-PtNi-B NSs are among the highest reported for Pt-based ORR catalysts (Fig. 3c and Supplementary Table 7). To elucidate the role of B incorporation, Int-PtNi-B NSs with lower and higher B contents (Int-PtNi-B_{Low} NSs with 7.6% B and Int-PtNi-B_{High} NSs with 25.2% B) were benchmarked against the standard Int-PtNi-B NSs containing 14.3% B (Supplementary Fig. 18). All Int-PtNi-B NSs outperform B-free Int-PtNi NSs in ORR activity (Fig. 3d,e and Supplementary Fig. 19). However, Int-PtNi-B_{Low} and Int-PtNi-B_{High} NSs deliver mass activities of 2.82 and 4.51 A mg^{-1}_{Pt} and specific activities of 7.68 and 11.05 mA cm^{-2}, respectively, both inferior to those of the optimally B-incorporated standard Int-PtNi-B NSs. This volcano-type trend demonstrates that precise control of B-incorporation is critical for enhancing ORR performance. We further examined the ORR properties of the compositionally extended Int-PtM-B NSs (Supplementary Fig. 20). Int-PtCo-B, Int-PtFe-B, and Int-PtMn-B NSs exhibit substantially higher catalytic activities for ORR than B-free catalysts. Although Int-PtNi-B NSs display the highest activity within the Int-PtM-B NSs, the consistently enhanced ORR performance of all Int-PtM-B NSs demonstrates that the present strategy provides a versatile platform for tuning catalytic properties through the selection of the constituent transition metal.

The ORR stability of the catalysts was evaluated by potential cycling between 0.6 and 1.0 V_{RHE} in O_2-saturated $HClO_4$. The polarization curve of Int-PtNi-B NSs shows an 8 mV shift in $E_{1/2}$ after 100,000 cycles (Fig. 3f), whereas Int-PtNi NSs, PtNi NSs, and Pt/C exhibit larger $E_{1/2}$ decays of 15, 29, and 81 mV, respectively (Supplementary Fig. 21 and Fig. 3g). Furthermore, Int-PtNi-B NSs exhibit only a 22.8% loss in mass activity at the end-of-life (Fig. 3h), in contrast to the larger decreases of 38.4% for Int-PtNi NSs, 60.5% for PtNi NSs, and 79.6% for Pt/C, respectively (Supplementary Fig. 22). Notably, after 100,000 cycles, the 2D morphology, intermetallic phase, and composition of Int-PtNi-B NSs were well-preserved (Supplementary Fig. 23). Chronoamperometry at 0.9 V_{RHE} and 60°C further confirms the superior durability of Int-PtNi-B NSs, which retained 99.6% of initial current after 720 h (Fig. 3i,j). By comparison, Int-PtNi NSs shows a more pronounced decline, while commercial Pt/C and PtNi NSs suffered severe degradation with losses of 99.9% and 60.1%, respectively (Fig. 3i,j). This exceptional durability arises from the combined enthalpic stability of ordered Pt–Ni bonding and Pt/Ni–B interactions, which suppress metal dissolution under operation.

Origin of the enhanced ORR performance

To elucidate the origin of enhanced ORR activity of the Int-PtNi-B NSs, we monitored surface intermediates using *in-situ* electrochemical Raman spectroscopy. Upon cathodic polarization, a new band appears at 720–732 cm^{-1} region, corresponding to the O–O stretching vibration of adsorbed *OOH[72,73]. Notably, this *OOH signature appears at 0.9 V_{RHE} for both Int-PtNi-B and Int-PtNi NSs (Fig. 4a and Supplementary Fig. 24), whereas disordered PtNi NSs and Pt/C require more negative potentials of 0.85 and 0.80 V_{RHE}, respectively, to generate detectable *OOH signals (Fig. 4b,c). The earlier onset potential of *OOH formation on the ordered surfaces indicates a lowered activation barrier for the initial O_2 adsorption and protonation step. The intensity of the *OOH band increases with decreasing potential, reflecting the potential-dependent surface coverage governed by proton-coupled electron transfer to adsorbed $*O_2$. For both ordered intermetallic catalysts, the *OOH signal reaches its maximum intensity at ~ 0.8 V_{RHE} and subsequently diminishes rapidly, becoming negligible below 0.6 V_{RHE}. In contrast, Pt/C and PtNi NSs retain substantial *OOH intensity even at 0.5 V_{RHE}. This accelerated *OOH consumption suggests more facile O–O bond cleavage and subsequent reduction. The combination of early *OOH formation and rapid *OOH conversion collectively accounts for the superior ORR kinetics observed on the ordered intermetallic catalysts.

To further resolve the different ORR activities of prepared catalysts, density functional theory (DFT) calculations were performed on Pt(111), Int-PtNi(111), and Int-PtNi-B(111) surfaces. As shown in the Gibbs free energy diagrams (Fig. 4d), interstitial B-incorporation weakens the binding strength of reaction intermediates, particularly O*, thereby alleviating the overly strong O* adsorption that typically limits ORR kinetics on Pt-based surfaces[74]. This optimized binding energy shifts the potential-limiting step from the hydrogenation of O* (O* → OH*) on Int-PtNi to OOH* formation (O_2 → OOH*) on Int-PtNi-B. Consequently, Int-PtNi-B(111) exhibits the lowest overpotential of 0.76 V, outperforming both Int-PtNi

(0.81 V) and pure Pt (1.03 V). To comprehensively understand this enhancement, we decoupled the ligand effect from the strain effect using constructed strain-only models (Fig. 4e,f). Applying tensile strain results in a linear upshift of the d-band center (Fig. 4e) and monotonic rise in the overpotential (Fig. 4f). Specifically, a tensile strain of 2.0% in Int-PtNi(111), consistent with the 2.0% lattice expansion observed experimentally for Int-PtNi-B NSs (Fig. 1n and Supplementary Fig. 25), results in an upshift of the d-band center from − 2.50 to -2.30 eV, indicating strengthened adsorption of oxygenated intermediates. According to the established strain–overpotential trend (Fig. 4f), lattice expansion would be expected to increase the overpotential by ~ 0.1 V due to excessive O* stabilization. However, despite identical ~ 2.0% tensile strain, the Int-PtNi-B exhibits a downshifted d-band center of − 2.52 eV and a reduced overpotential (Fig. 4e,f and Supplementary Fig. 26). These results demonstrate that the B-induced ligand effect dominates over the tensile strain effect, compensating for the lattice-expansion penalty and thereby accounting for the superior ORR activity of Int-PtNi-B NSs.

To elucidate the atomistic origin of the enhanced stability in Int-PtNi-B NSs, we calculated energy barriers for metal migration pathways (subsurface-to-surface and top-layer-to-adatom-layer migration). The Int-PtNi-B model consistently exhibits higher migration barriers than the reference systems (Fig. 5a,b, and Supplementary Fig. 27,28). This enhanced stability is attributed to strong metal–B interactions that effectively anchor Pt and Ni atoms within the lattice. Electronic structure analysis based on the electron localization function (ELF) reveals pronounced electron localization between B and adjacent metal atoms, indicative of covalent-like bonding, which is absent in the B-free Int-PtNi model (Fig. 5c). These covalent-like metal–B interactions increase the activation barriers for atomic migration, thereby suppressing surface reconstruction, and dissolution under operation.

To experimentally probe the structural robustness of the catalysts, *in-situ* X-ray absorption fine structure (XAFS) measurements were performed on PtNi, Int-PtNi, and Int-PtNi-B NSs at 0.1 and 0.9 V_{RHE}. At the Ni K-edge, disordered PtNi NSs exhibit a pronounced reduction in white-line intensity upon potential cycling (Fig. 5d), indicating substantial perturbation of the local Ni environment. In contrast, both Int-PtNi and Int-PtNi-B NSs display negligible white-line variation at both the Ni K-edge and Pt L_3-edge across the applied potentials (Fig. 5e,f and Supplementary Fig. 29), demonstrating that intermetallic ordering effectively stabilizes the metal coordination environment against potential-driven oxidation. This stabilization is further corroborated by quantitative EXAFS fitting (Fig. 5g-i, Supplementary Figs. 30–32, and Supplementary Tables 4–6). For disordered PtNi NSs, oxygen-associated coordination paths show pronounced potential dependence, with CN(Pt–O) increasing from 0.3 at 0.1 V_{RHE} to 0.7 at 0.9 V_{RHE}, and CN(Ni–O) rising from 0.9 to 1.5 over the same potential range. This behavior reflects that, in the disordered alloy, the catalyst surface undergoes a dynamic reconfiguration involving O-containing surface intermediates during the ORR. Consistently, the Debye-Waller factor (σ^2) associated with the Ni–Ni path shows more noticeable variation compared to those for Pt–Pt and Pt–Ni paths (Supplementary Table 4), pointing to a labile Ni environment in the disordered phase. In contrast, both Int-PtNi and Int-PtNi-B NSs reveal negligible metal–O contributions and retain invariant alloy-like coordination features (heterometallic fractions and bond distances of Pt–Ni and Ni–Pt paths) across the applied potentials

(Fig. 5j, Supplementary Tables 5,6). Taken together, intermetallic ordering provides the principal resistance to potential-induced oxidation and coordination changes, as experimentally demonstrated by XAFS, while interstitial B selectively increases metal migration barriers through covalent-like Pt/Ni–B interactions. This additional atomistic stabilization is consistent with the superior long-term durability of Int-PtNi-B NSs relative to B-free Int-PtNi NSs.

Conclusions

We report a sequential template-mediated strategy that independently controls intermetallic ordering and interstitial nonmetal incorporation, enabling the formation of Int-PtNi-B NSs with long-range Pt–Ni ordering and ultrathin NSs. The applicability of this approach to Int-PtCo-B, Int-PtFe-B, and Int-PtMn-B NSs further demonstrates its compositional versatility beyond the PtNi system. Establishing enthalpically stable Pt–Ni bonding prior to B incorporation is critical, as it suppresses Pt/Ni diffusion during B-incorporation and enables precise atomic-level modulation of metal–metal and metal–nonmetal interactions. The Int-PtNi-B NSs deliver exceptional ORR activity and durability, substantially outperforming disordered and B-free counterparts. *In-situ* XAFS, supported by DFT calculations, reveal that intermetallic ordering reinforced by covalent-like Pt/Ni–B interactions increases atomic migration barriers and suppresses potential-driven oxidation, and surface reconstruction. In parallel, interstitial B-incorporation induces a dominant ligand effect that overcomes the tensile-strain penalty, thereby optimizing oxygen-intermediate adsorption energetics. By integrating intermetallic ordering with interstitial nonmetal engineering in ultrathin 2D architectures, this work establishes a generalizable design principle for electrocatalysts that achieve enhanced activity and durability concurrently, with implications extending to broader electrochemical energy-conversion systems.

Methods

Chemicals and Materials

Potassium tetrachloroplatinate(II) (K_2PtCl_4, 99.0%), nickel(II) chloride hexahydrate ($NiCl_2{\cdot}6H_2O$, 99.9%) cetyltrimethylammonium chloride solution (CTAC, solution in water, 25 wt%), borane-tetrahydrofuran complex ($BH_3{\cdot}$THF, 1.0 M solution in THF), tetraethyl orthosilicate (TEOS, ≥ 98%), ammonia solution ($NH_3.H_2O$, ~ 28 wt%), and 11-mercaptoundecanoic acid (MUA, ≥ 95%), perchloric acid ($HClO_4$, 70%), isopropanol (IPA, > 99.99%), polyvinylpyrrolidone (PVP, Mw ~ 55,000), and Nafion solution (5 wt%) were purchased from Sigma-Aldrich. Pt/C (20 wt%, average Pt particle size = 3 nm) was purchased from Alfa Aesar. Hydrochloric acid (HCl, 37%) and L-ascorbic acid (AA, 99.5%) were purchased from Daejung. Lithium fluoride (LiF, ≥ 99%) and N,N-dimethylformamide (DMF, 99.5%) were purchased from Junsei. Deionized water (18.2 MΩ cm) was employed to prepare all reaction solutions.

Synthesis of Pt NSs

In a typical procedure, 4 mL of H_2O, 0.5 mL of DMF, 50 μL of 100 mM CTAC, and 20 mg of PVP were added into a vial under stirring. Subsequently, 1.5 mL of 5 mM K_2PtCl_4 solution and 0.5 mL of 100 mM AA were introduced into the mixture. The reaction was conducted at 40°C in a water bath for 1 h. After completion, the products were collected by centrifugation at 7000 rpm for 10 min and washed three times with ethanol.

Synthesis of PtM NSs (M = Ni, Co, Fe, and Mn)

PtNi, PtCo, PtFe, and PtMn NSs were prepared via a hydrothermal method. Briefly, 5 mg of the as-prepared Pt NSs were dispersed in a mixture of 1 mL of 37.5 mM $NiCl_2{\cdot}6H_2O$, $CoCl_2{\cdot}6H_2O$, $FeCl_2{\cdot}4H_2O$, or $MnCl_2{\cdot}4H_2O$ and 20 mg of PVP in a Teflon-lined autoclave. Subsequently, 0.5 mL of 100 mM AA was added under stirring. The mixture was then subjected to hydrothermal treatment at 180°C for 6 h. After cooling to room temperature, the products were collected by centrifugation at 7000 rpm for 5 min and washed three times with ethanol.

Synthesis of PtM@SiO_2 NSs

To coat the PtM NSs with SiO_2, 5 mg of the as-prepared PtM NSs was dispersed in a solution containing 80 μL of MUA, 35 mL of ethanol, and 4 mL of 22.4 mM TEOS. The mixture was aged at 60°C for 1 h, followed by stirring at room temperature for 10 min. Subsequently, 1 mL of the ammonia solution was added, and the reaction was maintained under stirring at room temperature for 18 h. The resulting PtM@SiO_2 NSs were collected by centrifugation at 7000 rpm for 5 min and washed three times with ethanol.

Synthesis of Int-PtM NSs

The as-prepared PtM@SiO_2 NSs were subjected to thermal annealing at 600°C under Ar/5% H_2 atmosphere for 6 h to obtain ordered intermetallic PtM NSs. After annealing, the samples were naturally cooled to room temperature.

Removal of SiO_2 shell

The SiO_2 shell was removed by chemical etching. Typically, the annealed PtM@SiO_2 NSs were dispersed in a mixed solution containing 0.3 g of LiF and 60 mL of 3 M HCl. The suspension was stirred at 50°C for 5 h to completely remove the SiO_2 layer. The resulting products were collected by centrifugation and washed three times with deionized water.

Synthesis of Int-PtM-B NSs

Interstitial B was incorporated via solvothermal treatment. The Int-PtM NSs were dispersed in a solution of borane–tetrahydrofuran (BH_3 . THF) and transferred into a Teflon-lined autoclave. The reaction was

conducted at 180°C for 7 days. After cooling to room temperature, the products were collected by centrifugation and washed thoroughly with ethanol.

Preparation of the working electrode.

Before estimating the electrocatalytic properties of the catalysts, they were supported on a carbon support (Vulcan XC 72) with a Pt loading of about 20 wt%, determined through ICP-OES. In detail, an ethanol suspension (15 mL) including as-synthesized catalysts was added to another 20 mL of an ethanol suspension containing carbon support (30 mg). The mixture was then sonicated for 5 h, followed by overnight stirring. Subsequently, the carbon-supported catalysts were collected via centrifugation, redispersed in 10 mL of acetic acid, and heated at 60 ^{o}C for 3 h to remove the chemically adsorbed species on the surface of the catalysts. Finally, the catalysts were retrieved through centrifugation, rinsed with ethanol, and dried overnight in an oven. For the preparation of catalyst ink, catalyst (~ 2.5 mg) was dissolved in a mixture solution (1.25 mL) of DI water (1.0 mL), isopropyl alcohol (0.24 mL), and Nafion solution (10 µL, 5 wt%). The mixture was then sonicated for 1 h to prepare a highly dispersed catalyst ink. The final concentration of Pt in the as-prepared catalyst ink was determined to be 0.4 $\mu g_{Pt}\ \mu L^{-1}$. A working electrode was prepared by loading 10 µL of the catalyst ink on a pre-cleaned glassy carbon rotating disk electrode (RDE, 0.196 cm^2 in geometric area, Pine Research Instrumentation) and dried in an oven. The commercial Pt/C (20 wt%) was prepared with the same protocol and used for comparison. Finally, the total Pt mass loadings on working electrode for all catalysts was 20.4 $\mu g\ cm^{-2}$.

Electrochemical measurement

All the electrochemical measurements were performed in three-electrode cells using EC-Lab Biologic Model SP-300 potentiostat at room temperature. Graphite rods and Ag/AgCl (1.0 M KCl) were used as the counter and reference electrodes, respectively. For the ORR measurement, Pine Research Instrumentation, with a rotating disk electrode containing a glassy carbon disk (RDE, GC, 5 mm in diameter with a geometric area of 0.196 cm^2, E3TPK) used as a working electrode and connected into the potentiostat. Prior to electrochemical experiments, RDE was polished with 0.05 µm Al_2O_3 bead solution and cleaned with deionized water. Cyclic voltammetry (CV) was conducted in a potential cycle between 0.08 to 1.108 V_{RHE} in an N_2-saturated 0.1 M $HClO_4$ solution for 50 cycles at a scan rate of 100 $mV\ s^{-1}$ and final CV was recorded at a scan rate of 50 $mV\ s^{-1}$. Hydrogen underpotential deposition (H_{upd}) based electrochemical surface area (ECSA) was measured from CV curves, where from H_{upd} adsorption/desorption peak areas appeared in the region from 0.08 and 0.40 V_{RHE}. The charges (Q_H) associated with averaging adsorption/ desorption region were divided with a reference value of 210 $\mu C\ cm^{-2}$ and then again with the total mass of Pt loading.

ORR measurements were conducted in an O_2-saturated 0.1 M $HClO_4$ solution with a scan rate of 10 $mV\ s^{-1}$ and rotated with a rotation speed of 1600 rpm. ORR polarization curves were iR-compensated. The Koutecky-Levich equation was used to obtain kinetic current density (j_k):

$$\frac{1}{j_m} = \frac{1}{j_k} + \frac{1}{j_l}$$

$j_k = \frac{(j_m \times j_l)}{j_l - j_m}$

Where, j_m and j_l are the measured current density and the diffusion limiting current, respectively.

Accelerated durability test (ADT) was conducted in an O_2-saturated 0.1 M $HClO_4$ solution, where potential was cycled for 100,000 cycles between 0.6 and 1.0 V_{RHE} at a rate of 100 mV s^{-1}. After 100,000 cycles of ADT, the CV and ORR polarization curves were measured again in a fresh 0.1 M $HClO_4$ solution. To further determine the electrochemical stability, chronoamperometry at potential 0.9 V_{RHE} in 0.1 M $HClO_4$ was used to monitor the change of current with time for 720 h at 60 ^oC under high purity O_2 bubbling into the solution at a constant rate.

Characterizations

Transmission electron microscopy (TEM) and scanning electron microscopy (SEM) images of the synthesized samples were obtained using a JEOL JEM-2100F and JEOL JSM-7210F, respectively. Inductively coupled plasma optical emission spectrometry (ICP-OES) was performed using an Ametek ICP-OES instrument. X-ray diffraction (XRD) patterns were recorded on a Rigaku D/MAX2500V/PC diffractometer over a 2θ range of 20°–90°. Lattice parameters were calculated from the XRD peak positions using Bragg's law, and the lattice strain was determined from the relative change in the lattice parameter. X-ray photoelectron spectroscopy (XPS) measurements were carried out using a Thermo VG Scientific Sigma Probe spectrometer equipped with an Al Kα X-ray source (1486.6 eV). The binding energies were calibrated to the C 1s peak at 284.5 eV. Prior to XPS analysis, samples were etched with Ar for 30 s to remove surface-adsorbed species. For TEM sample preparation, residual chemicals in the samples dispersion were removed by centrifugation. The collected precipitate was redispersed in deionized water, and a drop of the suspension was cast onto a carbon-coated copper TEM grid (Lacey/Carbon 300 mesh, Copper). The grid was air-dried at room temperature prior to imaging. TEM grids were rinsed with ethanol before use.

In-situ electrochemical Raman spectroscopy

In-situ electrochemical Raman measurements were performed using an inVia Qontor Raman microscope (Renishaw) equipped with a 638 nm excitation laser with a laser power 50 mW. The experiments were conducted in a homemade spectro-electrochemical cell using a catalyst-coated Si-coated Au electrode as the working electrode, a graphite rod as the counter electrode, and an Ag/AgCl electrode as the reference electrode. Before the measurements, 20 µL of catalyst ink was drop-cast onto the working electrode and dried naturally. The electrode potential was controlled using an EC-Lab Biologic Model SP-300 potentiostat operated with EC-Lab software, and Raman spectra were collected under potentiostatic

conditions over the potential range of 0.40–1.00 V versus RHE in 0.1 M $HClO_4$. All potentials were converted to the RHE scale and corrected for the iR drop.

XAFS analyses

XAFS analyses at the Pt L_3-edge and Ni K-edge were conducted to obtain the physicochemical information of Pt and Ni in the PtNi catalysts at different states (i.e., pristine state and electrochemical potentials at 0.9 V_{RHE} and 0.1 V_{RHE}). A lab-made acryl kit was used for the *in-situ* analysis.[75,76] The XAFS measurements were conducted at a 10C beamline (Wide XAFS) in Pohang Light Source-II (PLS-II) at Pohang Accelerating Laboratory (PAL), Republic of Korea. The storage ring was operated in a top-up mode at an energy of 3.0 GeV and an operating current of 250 mA. XAFS spectra were obtained at room temperature under fluorescence mode by using a double-crystal monochromator (Si(111)) detuned to 75% of its maximum intensity to avoid unwanted high-order harmonics. The energy of each spectrum was calibrated using the edge energy of the corresponding metal foils (8333 eV for Ni and 11564 eV for Pt) that were recorded simultaneously.

The ATHENA and ARTEMIS software in the IFEFFIT package were utilized in analyzing the obtained spectra to yield XANES and EXAFS profiles. Detailed data processing was conducted in accordance with the procedures described in previous reports[77–79]. EXAFS spectrum ($\chi(k)$) was weighted by k^3 to intensify the oscillation in the high *k* regime. Note that the radial distances in the Fourier-transformed (FT) EXAFS spectra are presented as phase-uncorrected apparent distances while the fitted bond lengths correspond to real interatomic distances after phase correction during EXAFS fitting. Amplitude reduction factor (S_o^2) values were obtained by using the corresponding metal foils. The Hanning window was used for Fourier transform into *R*-space (Å). All EXAFS fittings were performed in *R*-space. The reliability factor (R-factor) and reduced χ^2 were used to evaluate the goodness of fit.

The areal loading of the working electrode was ~ 5 $mg_{catalyst}$ cm^{-2}. During the measurement, O_2 gas was continuously supplied into the electrolyte. The working electrode potential was controlled by an RHE (Hydroflex, EDAQ), and highly oriented pyrolytic graphite paper was used as a counter electrode. The other conditions were the same as in the electrochemical measurements. The structure models for the EXAFS fitting are provided in Supplementary Table 2.

DFT calculation

Density functional theory (DFT) calculations were performed using the Vienna Ab initio Simulation Package (VASP, version 5.4.4). The ion-electron interactions were described by the projector augmented-wave (PAW) method. The exchange-correlation energy was treated using the generalized gradient approximation (GGA) with the Perdew-Burke-Ernzerhof (PBE) functional. A plane-wave basis set with a kinetic energy cutoff of 500 eV was employed for all calculations.

The bulk structures of Pt, Int-PtNi, and Int-PtNi-B were optimized using a gamma-centered 16 × 16 × 16 k-points mesh. For the Int-PtNi, Pt atoms were symmetrically substituted with Ni atoms to form an

equiatomic structure. The Int-PtNi-B structure was generated by placing a boron atom at the interstitial site, surrounded by Ni atoms.

Subsequently, the (111) surface models were constructed using a 4 × 4 supercell with a thickness of six atomic layers. Pt-skin terminations were imposed by substituting the outermost atomic layer of the Int-PtNi(111) and Int-PtNi-B(111) slabs with Pt atoms. To prevent spurious interactions between periodic images, a vacuum layer of approximately 20 Å was applied along the z-direction. The Brillouin zone for the surface slab was sampled using a gamma-centered 4 × 4 × 1 k-points mesh. During structural relaxation, the bottom two atomic layers were constrained to the optimized bulk positions to simulate the bulk environment, while the upper four layers and adsorbates were allowed to relax fully.

Reaction free energies were evaluated using the computational hydrogen electrode (CHE) approach (vs RHE), where the chemical potential of a proton-electron pair ($H^+ + e^-$)) was referenced to half the chemical potential of H_2(g). The Gibbs free energy change was calculated at 298.15 K as:

$$\Delta G(U) = \Delta E_{DFT} + \Delta ZPE - T\Delta S - neU$$

where ΔE_{DFT}, ΔZPE and ΔS represent the changes in total DFT energy, zero-point energy, and entropy, respectively. n is the number of transferred electrons. The ΔZPE and T ΔS terms were evaluated using the ASE thermochemistry module, modeling adsorbates under the harmonic approximation and gas-phase molecules under the ideal-gas approximation.

Declarations

Competing interests

The authors declare no competing interests.

Additional information

All data supporting the findings of this study are available within the Article and its Supplementary Information. Source data are provided with this paper.

TOC

Data availability

All data supporting the findings of this study are available within the paper and its Supplementary Information.

References

1. Wu, X. *et al.* Heterostructured Catalytic Materials as Advanced Electrocatalysts: Classification, Synthesis, Characterization, and Application. *Adv. Funct. Mater.* 34, 2404535 (2024).
2. Wu, N., Shi, W., Wang, W. & Lei, Y. Well-Defined Nanostructures: Concept, Impact and Perspective. *Small* 22, 2412780 (2026).
3. Begley, M. R., Gianola, D. S. & Ray, T. R. Bridging functional nanocomposites to robust macroscale devices. *Science* 364, 1250 (2019).
4. Ha, M. *et al.* Multicomponent Plasmonic Nanoparticles: From Heterostructured Nanoparticles to Colloidal Composite Nanostructures. *Chem. Rev.* 119, 12208–12278 (2019).
5. Hammond, P. T. Enabling Nanoscience: From Computation to Experimental Assay Tools. *ACS Nano* 2, 811–812 (2008).
6. Nicole, L., Rozes, L. & Sanchez, C. Integrative Approaches to Hybrid Multifunctional Materials: From Multidisciplinary Research to Applied Technologies. *Adv. Mater.* 22, 3208–3214 (2010).
7. Jiang, B. *et al.* Nanoarchitectonics of Metallene Materials for Electrocatalysis. *ACS Nano* 17, 13017–13043 (2023).
8. Wang, Y., Zhang, Z., Mao, Y. & Wang, X. Two-dimensional nonlayered materials for electrocatalysis. *Energy Environ. Sci.* 13, 3993–4016 (2020).
9. Tan, C. *et al.* Recent Advances in Ultrathin Two-Dimensional Nanomaterials. *Chem. Rev.* 117, 6225–6331 (2017).
10. Ren, F. *et al.* Metallene: Ångström-Scale 2D Metals. *Adv. Mater.* 38, e12683 (2026).
11. Kabiraz, M. K., Wahidah, H., Hong, J. W. & Choi, S. Platinum Metallenes: Advanced Electrocatalysts for Sustainable Energy Solutions. *Small* 21, 2500858 (2025).
12. Wang, P., Zhao, D. & Yin, L. Two-dimensional matrices confining metal single atoms with enhanced electrochemical reaction kinetics for energy storage applications. *Energy Environ. Sci.* 14, 1794–1834 (2021).
13. Chen, L. X. *et al.* Insights on the dual role of two-dimensional materials as catalysts and supports for energy and environmental catalysis. *J. Mater. Chem. A* 9, 2018–2042 (2021).
14. Gao, Y. *et al.* Emerging Amorphized Metastable Structures to Break Limitations of 2D Materials for More Promising Electrocatalysis. *ACS Energy Lett.* 9, 3982–4002 (2024).
15. Wang, Y. *et al.* Catalysis with Two-Dimensional Materials Confining Single Atoms: Concept, Design, and Applications. *Chem. Rev.* 119, 1806–1854 (2019).
16. Zhang, M., Wang, Z., Bo, X., Huang, R. & Deng, D. Two-Dimensional Catalysts: From Model to Reality. *Angew. Chem. Int. Ed.* 64, e202419661 (2025).
17. Xue, D. *et al.* Spin Engineering of Dual-Atom Site Catalysts for Efficient Electrochemical Energy Conversion. *Adv. Mater.* 37, 2504213 (2025).
18. Han, A., Zhang, Z., Li, X., Wang, D. & Li, Y. Atomic Thickness Catalysts: Synthesis and Applications. *Small Methods* 4, 2000248 (2020).

19. Wu, X. *et al.* Emerging 2D Materials for Electrocatalytic Applications: Synthesis, Multifaceted Nanostructures, and Catalytic Center Design. *Small* 18, 2105831 (2022).
20. Lin, F., Li, M., Zeng, L., Luo, M. & Guo, S. Intermetallic Nanocrystals for Fuel-Cells-Based Electrocatalysis. *Chem. Rev.* 123, 12507–12593 (2023).
21. Deng, J., Deng, D. & Bao, X. Robust Catalysis on 2D Materials Encapsulating Metals: Concept, Application, and Perspective. *Adv. Mater.* 29, 1606967 (2017).
22. Li, H., Qin, X., Zhang, X.-G., Jiang, K. & Cai, W.-B. Boron-Doped Platinum-Group Metals in Electrocatalysis: A Perspective. *ACS Catal.* 12, 12750–12764 (2022).
23. Wang, Y., Lv, H., Sun, L. & Liu, B. Mesoporous Noble Metal–Metalloid/Nonmetal Alloy Nanomaterials: Designing Highly Efficient Catalysts. *ACS Nano* 15, 18661–18670 (2021).
24. Chen, L. *et al.* Metal boride better than Pt: HCP Pd_2B as a superactive hydrogen evolution reaction catalyst. *Energy Environ. Sci.* 12, 3099–3105 (2019).
25. Lv, X. *et al.* Engineering Orbital Hybridization in Advanced Electrocatalysts for Energy Conversion: Fundamentals, Modulations, and Perspectives. *Adv. Energy Mater.* 15, 2501129 (2025).
26. Chen, H. *et al.* d–sp orbital hybridization: a strategy for activity improvement of transition metal catalysts. *Chem. Commun.* 58, 7730–7740 (2022).
27. He, B., Xiang, X. & Zhu, M. Emerging Metallenes: Synthesis, Modification, and Application. *Small* 21, e05095 (2025).
28. Yu, Q. & Yang, Y. Synthesis of Two-dimensional Metallic Nanosheets: From Elemental Metals to Chemically Complex Alloys. *ChemNanoMat* 6, 1683–1711 (2020).
29. Liu, C. *et al.* Massive interstitial solid solution alloys achieve near-theoretical strength. *Nat. Commun.* 13, 1102 (2022).
30. Weertman, J. R. Retaining the Nano in Nanocrystalline Alloys. *Science (1979).* 337, 921–922 (2012).
31. Zhou, M., Li, C. & Fang, J. Noble-Metal Based Random Alloy and Intermetallic Nanocrystals: Syntheses and Applications. *Chem. Rev.* 121, 736–795 (2021).
32. Wen, Y. *et al.* A Coherent Pd–$Pd_{16}B_3$ Core–Shell Electrocatalyst for Controlled Hydrogenation in Nitrogen Reduction Reaction. *Adv. Funct. Mater.* 34, 2400849 (2024).
33. Ding, Y., Huang, Y., Li, Y., Zhang, T. & Wu, Z. Regulating surface electron structure of PtNi nanoalloy via boron doping for high-current-density Li-O_2 batteries with low overpotential and long-life cyclability. *SmartMat* 5, e1150 (2024).
34. Han, P. *et al.* An Interstitial Boron Inserted Metastable Hexagonal Rh Nanocrystal for Efficient Hydrogen Oxidation Electrocatalysis. *Angew. Chem. Int. Ed.* 64, e202419320 (2025).
35. Xu, W. *et al.* Nitrogen doping to accelerate the phase transition to ordered intermetallic Pt_3Co catalyst for the oxygen reduction reaction in fuel cells. *J. Mater. Chem. A* 11, 4078–4087 (2023).
36. Zhao, X. *et al.* High-Performance Nitrogen-Doped Intermetallic PtNi Catalyst for the Oxygen Reduction Reaction. *ACS Catal.* 10, 10637–10645 (2020).

37. Li, J. *et al.* Anisotropic Strain Tuning of $L1_0$ Ternary Nanoparticles for Oxygen Reduction. *J. Am. Chem. Soc.* 142, 19209–19216 (2020).
38. Chen, S.-M. *et al.* Electronegativity of Doped Metals Determines the Stability of PtFeM Intermetallic Catalysts for Oxygen Reduction Reaction. *ACS Energy Lett.* 10, 6401–6407 (2025).
39. Lu, F. *et al.* Structurally Ordered High-Entropy Intermetallics for Electrocatalysis. *Adv. Energy Mater.* 15, e03306 (2025).
40. Gamler, J. T. L., Ashberry, H. M., Skrabalak, S. E. & Koczkur, K. M. Random Alloyed versus Intermetallic Nanoparticles: A Comparison of Electrocatalytic Performance. *Adv. Mater.* 30, 1801563 (2018).
41. Mun, J. H. *et al.* Monodisperse Pattern Nanoalloying for Synergistic Intermetallic Catalysis. *Nano Lett.* 13, 5720–5726 (2013).
42. Xiao, W., Lei, W., Gong, M., Xin, H. L. & Wang, D. Recent Advances of Structurally Ordered Intermetallic Nanoparticles for Electrocatalysis. *ACS Catal.* 8, 3237–3256 (2018).
43. Yan, Y. *et al.* Intermetallic Nanocrystals: Syntheses and Catalytic Applications. *Adv. Mater.* 29, 1605997 (2017).
44. Lin, C. *et al.* Creating Atomic Ordering in Electrocatalysis. *Adv. Funct. Mater.* 33, 2212827 (2023).
45. Campos-Roldán, C. A. *et al.* Dissolution Trends of Platinum-Based Intermetallic Nanocatalysts toward the Acidic Oxygen Reduction Reaction. *ACS Catal.* 15, 17950–17957 (2025).
46. Zhong, Z. *et al.* Surface Strain Effect on Electrocatalytic Hydrogen Evolution Reaction of Pt-Based Intermetallics. *ACS Catal.* 14, 2917–2923 (2024).
47. Yang, C.-L. *et al.* Sulfur-anchoring synthesis of platinum intermetallic nanoparticle catalysts for fuel cells. *Science (1979)*. 374, 459–464 (2021).
48. Yang, C. *et al.* Metal Alloys-Structured Electrocatalysts: Metal–Metal Interactions, Coordination Microenvironments, and Structural Property–Reactivity Relationships. *Adv. Mater.* 35, 2301836 (2023).
49. Cao, X. *et al.* Sandwiching intermetallic Pt_3Fe and ionomer with porous N-doped carbon layers for oxygen reduction reaction. *Nat. Commun.* 16, 2851 (2025).
50. Hou, Y. *et al.* Synergistic Modulation of Multiple Sites Boosts Anti-Poisoning Hydrogen Electrooxidation Reaction with Ultrasmall $(Pt_{0.9}Rh_{0.1})_3V$ Ternary Intermetallic Nanoparticles. *Angew. Chem. Int. Ed.* 63, e202402496 (2024).
51. Feng, F. *et al.* Breaking Highly Ordered PtPbBi Intermetallic with Disordered Amorphous Phase for Boosting Electrocatalytic Hydrogen Evolution and Alcohol Oxidation. *Angew. Chem. Int. Ed.* 63, e202405173 (2024).
52. Luo, M., Sun, Y., Wang, L. & Guo, S. Tuning Multimetallic Ordered Intermetallic Nanocrystals for Efficient Energy Electrocatalysis. *Adv. Energy Mater.* 7, 1600148 (2017).
53. Liang, J. *et al.* Metal bond strength regulation enables large-scale synthesis of intermetallic nanocrystals for practical fuel cells. *Nat. Mater.* 23, 1259–1267 (2024).

54. Wang, Z. *et al.* Structurally Ordered Low-Pt Intermetallic Electrocatalysts toward Durably High Oxygen Reduction Reaction Activity. *Adv. Funct. Mater.* 29, 1902987 (2019).
55. Zhang, L. *et al.* Optimized Surface Strain in $L1_0$-Type $Pt_{0.8}Ga_{0.2}Co$ Intermetallic Catalyst for Enhanced Oxygen Reduction in Fuel Cells. *Chem. Mater.* 36, 11404–11411 (2024).
56. Zhao, W., Hu, Z., Li, M. & Hu, S. Asymmetrical Promotional Effect in the Disorder-to-Order Transition of Au-Pt-Cu Ternary Alloy Electrocatalysts. *Adv. Funct. Mater.* 34, 2409481 (2024).
57. Maulana, M. I. *et al.* Magnetocrystalline Anisotropic Platinum–Palladium–Iron Ternary Intermetallic Alloy for Enhanced Fuel Cell Electrocatalysis. *Adv. Mater.* 37, e10314 (2025).
58. Kim, H. Y. *et al.* Activity Origin and Multifunctionality of Pt-Based Intermetallic Nanostructures for Efficient Electrocatalysis. *ACS Catal.* 9, 11242–11254 (2019).
59. Cao, C., Xu, Q. & Zhu, Q.-L. Ultrathin two-dimensional metallenes for heterogeneous catalysis. *Chem Catalysis* 2, 693–723 (2022).
60. Liang, J. *et al.* Ultrathin and defect-rich intermetallic Pd_2Sn nanosheets for efficient oxygen reduction electrocatalysis. *J. Mater. Chem. A* 8, 15665–15669 (2020).
61. Zhan, G., Li, P. & Zeng, H. C. Nanocatalysts: Architectural Designs and Synthetic Strategies of Advanced Nanocatalysts (Adv. Mater. 47/2018). *Adv. Mater.* 30, 1870362 (2018).
62. Yang, Y. & Wei, M. Intermetallic compound catalysts: synthetic scheme, structure characterization and catalytic application. *J. Mater. Chem. A* 8, 2207–2221 (2020).
63. Chen, Y. *et al.* Pt Atomic Layers with Tensile Strain and Rich Defects Boost Ethanol Electrooxidation. *Nano Lett.* 22, 7563–7571 (2022).
64. Yang, Z., Yang, H., Shang, L. & Zhang, T. Ordered PtFeIr Intermetallic Nanowires Prepared through a Silica-Protection Strategy for the Oxygen Reduction Reaction. *Angew. Chem. Int. Ed.* 61, e202113278 (2022).
65. Xie, M. *et al.* Pt–Co@Pt Octahedral Nanocrystals: Enhancing Their Activity and Durability toward Oxygen Reduction with an Intermetallic Core and an Ultrathin Shell. *J. Am. Chem. Soc.* 143, 8509–8518 (2021).
66. Kim, H. Y. *et al.* Intermetallic PtCu Nanoframes as Efficient Oxygen Reduction Electrocatalysts. *Nano Lett.* 20, 7413–7421 (2020).
67. Ashberry, H. M., Gamler, J. T. L., Unocic, R. R. & Skrabalak, S. E. Disorder-to-Order Transition Mediated by Size Refocusing: A Route toward Monodisperse Intermetallic Nanoparticles. *Nano Lett.* 19, 6418–6423 (2019).
68. Liao, K. *et al.* Precise diameter control derived intermetallic PtNiCo nanowires: a simple two-step synthesis and *operando* XAS insight. *J. Mater. Chem. A* 14, 651–662 (2026).
69. Chen, H. *et al.* Effect of Atomic Ordering Transformation of PtNi Nanoparticles on Alkaline Hydrogen Evolution: Unexpected Superior Activity of the Disordered Phase. *J. Phys. Chem. C* 124, 5036–5045 (2020).

70. Chen, J., Finfrock, Y. Z., Wang, Z. & Sham, T.-K. High Energy Resolution Fluorescence Detection of the Pt $L_{3,2}$ -Edge Whitelines of Pt-Based Bimetallic Systems: Implications for the Pt $5d_{5/2,3/2}$ Density of States. *J. Phys. Chem. C* 125, 2327–2333 (2021).
71. Hlil, E. K., Baudoing-Savois, R., Moraweck, B. & Renouprez, A. J. X-ray Absorption Edges in Platinum-Based Alloys. 2. Influence of Ordering and of the Nature of the Second Metal. *J. Phys. Chem.* 100, 3102–3107 (1996).
72. Dong, J.-C. *et al.* In situ Raman spectroscopic evidence for oxygen reduction reaction intermediates at platinum single-crystal surfaces. *Nat. Energy* 4, 60–67 (2018).
73. Dong, J.-C. *et al.* Direct *In Situ* Raman Spectroscopic Evidence of Oxygen Reduction Reaction Intermediates at High-Index Pt(*hkl*) Surfaces. *J. Am. Chem. Soc.* 142, 715–719 (2020).
74. Mao, Z. *et al.* Interstitial B-Doping in Pt Lattice to Upgrade Oxygen Electroreduction Performance. *ACS Catal*. 12, 8848–8856 (2022).
75. Kim, M. S. *et al.* Ligand environment engineering of nickel single atomic sites for efficient electrochemical carbon dioxide reduction reaction. *J. Mater. Chem. A* 13, 3834–3848 (2025).
76. Lee, J. H. *et al.* Tuning the activity and selectivity of electroreduction of CO_2 to synthesis gas using bimetallic catalysts. *Nat. Commun.* 10, 3724 (2019).
77. Rehr, J. J. & Albers, R. C. Theoretical approaches to x-ray absorption fine structure. *Rev. Mod. Phys.* 72, 621–654 (2000).
78. Kelly, S. D., Hesterberg, D. & Ravel, B. Analysis of Soils and Minerals Using X-ray Absorption Spectroscopy. in 387–463 (2008).
79. Ravel, B. & Newville, M. ATHENA, *ARTEMIS*, *HEPHAESTUS*: data analysis for X-ray absorption spectroscopy using *IFEFFIT*. *J. Synchrotron Radiat.* 12, 537–541 (2005).

Figures

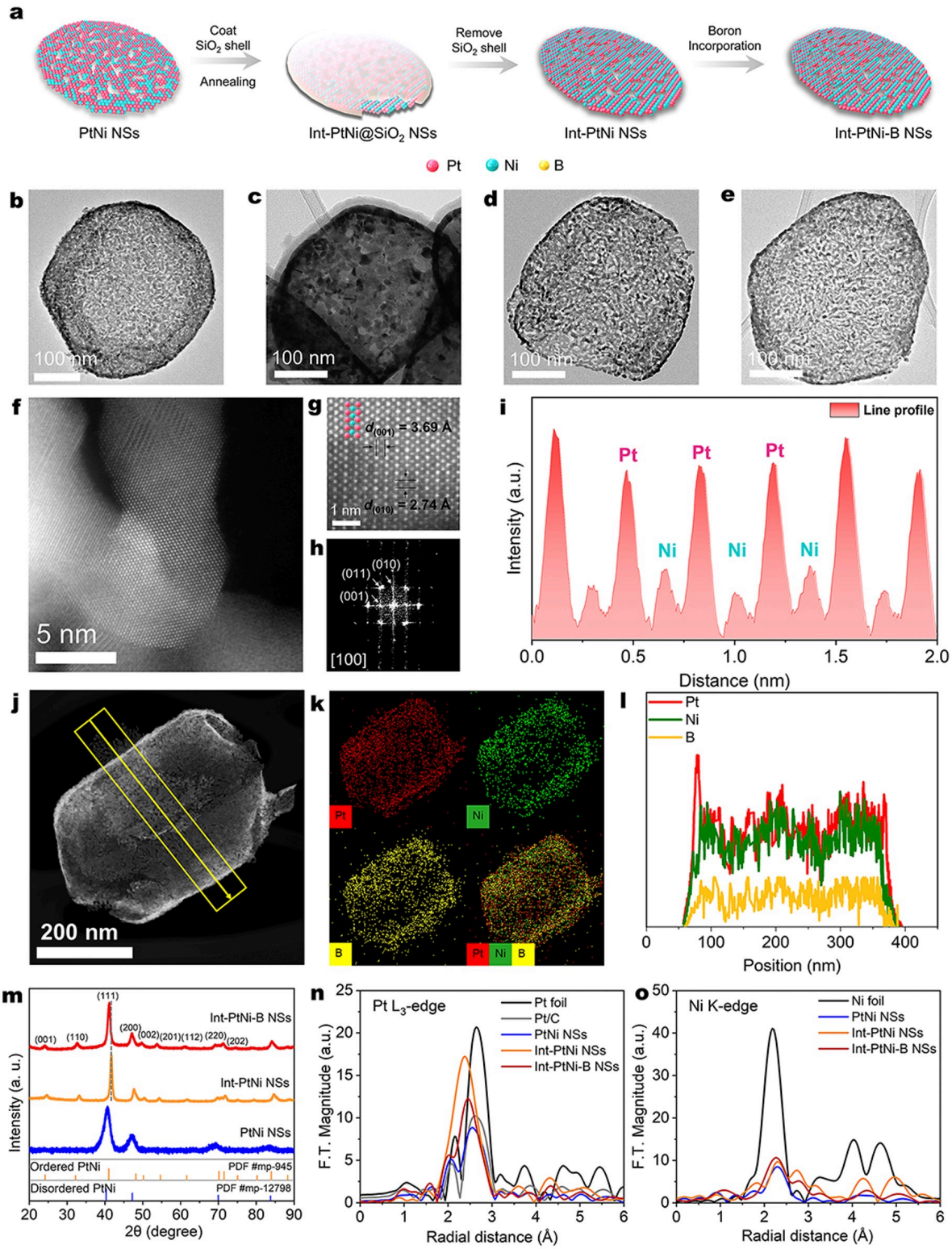


Figure 1

Synthesis and structural characterization of Int-PtNi-B NSs. a, Schematic illustration of the synthesis process for Int-PtNi-B NSs, including SiO_2 coating, thermal annealing to induce intermetallic ordering, SiO_2 removal, and subsequent B incorporation. **b–e**, TEM images showing the morphological evolution from PtNi NSs (**b**) to Int-PtNi@SiO_2 NSs (**c**), Int-PtNi NSs after SiO_2 removal (**d**), and Int-PtNi-B NSs (**e**). **f**, HAADF-STEM image of Int-PtNi-B NSs. **g**, Atomic-resolution HAADF-STEM image revealing the ordered

atomic arrangement, with corresponding interplanar spacings. **h**, Fast Fourier transform (FFT) pattern indexed to the $L1_0$ intermetallic structure. **i**, Intensity line profile along the marked direction in h, showing alternating Pt and Ni atomic columns. **j**, HAADF-STEM image of Int-PtNi-B NSs with the region selected for elemental mapping. **k**, Energy-dispersive X-ray spectroscopy (EDS) elemental maps of Pt, Ni, and B, and their overlay, confirming uniform elemental distribution. **l**, Corresponding line-scan profiles of Pt, Ni, and B along the marked region in k, verifying the successful incorporation of B. **m**, XRD patterns showing the transition from disordered PtNi to ordered intermetallic PtNi and Int-PtNi-B NSs. **n**,**o**, Fourier-transformed EXAFS spectra at the Pt L_3-edge (**n**) and Ni K-edge (**o**), confirming the evolution of local coordination environments and intermetallic ordering.

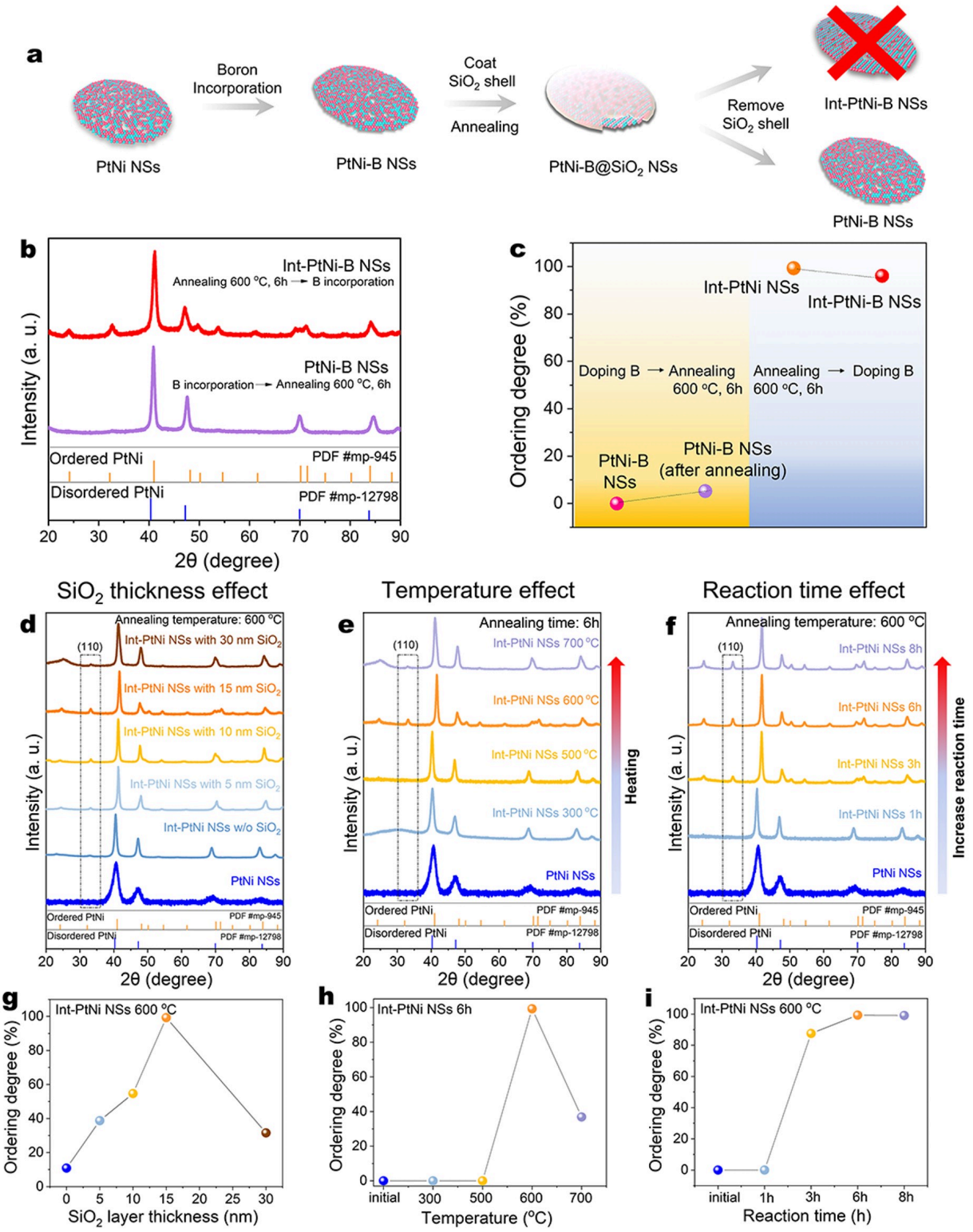


Figure 2

Formation mechanism and ordering control of Int-PtNi-B NSs. a, Schematic illustration of the effect of B incorporation sequence on intermetallic phase formation. **b**, XRD patterns comparing disordered PtNi NSs, PtNi-B NSs (B incorporation before annealing), and Int-PtNi-B NSs (annealing followed by B incorporation), highlighting the evolution of intermetallic ordering. **c**, Comparison of ordering degree under different synthesis sequences, showing that intermetallic ordering is maximized when B

incorporation is performed after annealing. **d**, Effect of SiO_2 shell thickness on intermetallic ordering, as revealed by XRD patterns. **e**, Temperature-dependent evolution of intermetallic ordering, showing enhanced ordering with increasing annealing temperature. **f**, Reaction time-dependent evolution of intermetallic ordering at 600 °C, indicating progressive ordering with prolonged annealing time. **g–i**, Quantitative analysis of ordering degree as a function of SiO_2 thickness (**g**), annealing temperature (**h**), and reaction time (**i**), respectively.

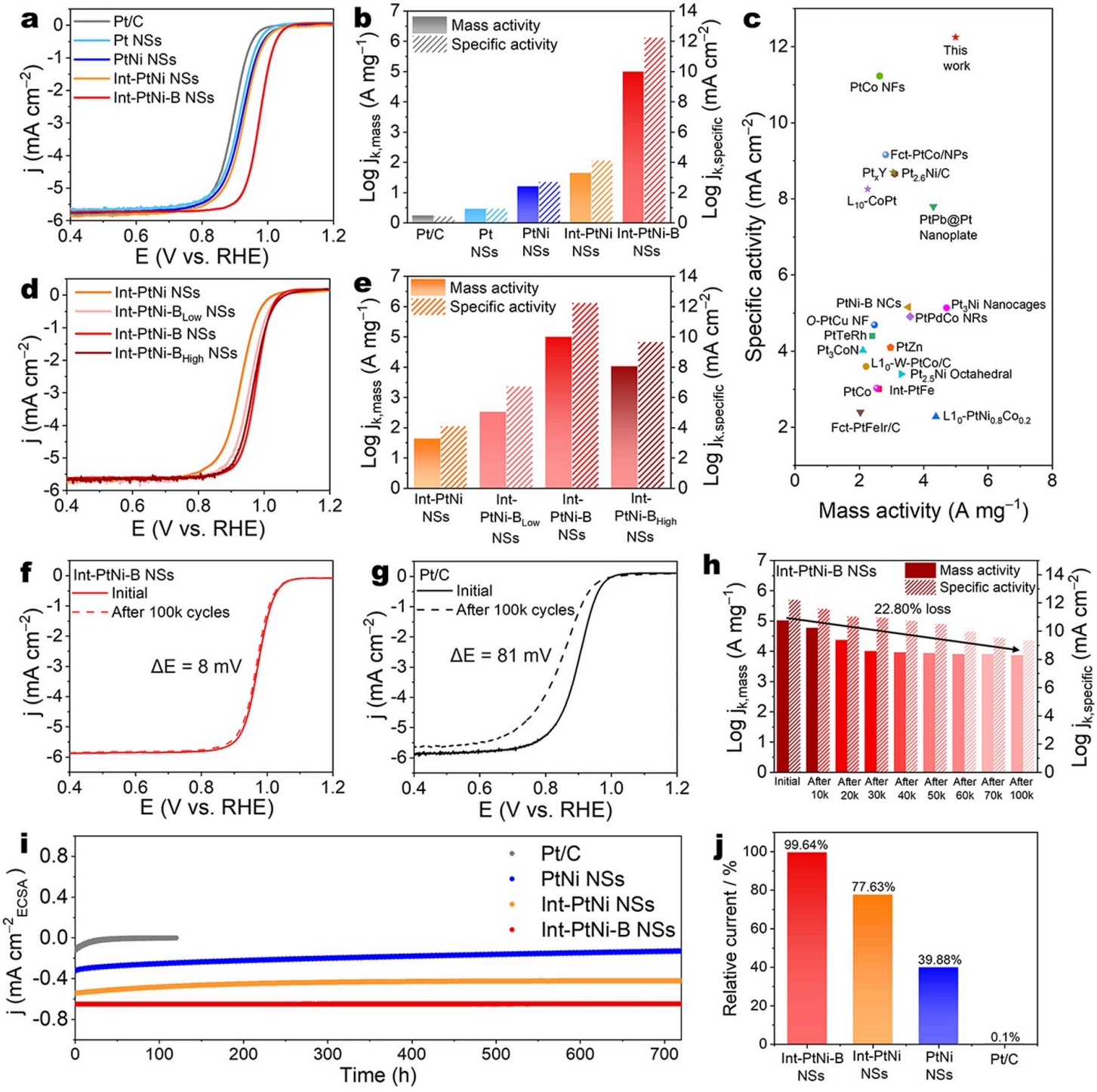


Figure 3

Electrocatalytic ORR performance and durability. a, LSV curves of Pt/C, PtNi NSs, Int-PtNi NSs, and Int-PtNi-B NSs in O_2-saturated 0.1 M $HClO_4$. **b**, Corresponding mass and specific activities at 0.9 V_{RHE}. **c**, Benchmark comparison of ORR activity (mass and specific activities) of Int-PtNi-B NSs with previously reported Pt-based electrocatalysts. **d,e**, Influence of B-incorporation on ORR activity: LSV curves (d) and corresponding mass and specific activities (e) of Int-PtNi NSs with varying B contents. **f,g**, ADT: LSV curves of Int-PtNi-B NSs (f) and Pt/C (g) before and after 100,000 potential cycles. **h**, Evolution of mass and specific activities of Int-PtNi-B NSs during durability cycling. **i**, Chronoamperometry stability over extended operation for Pt/C, PtNi NSs, Int-PtNi NSs, and Int-PtNi-B NSs. **j**, Relative current retention after long-term stability testing.

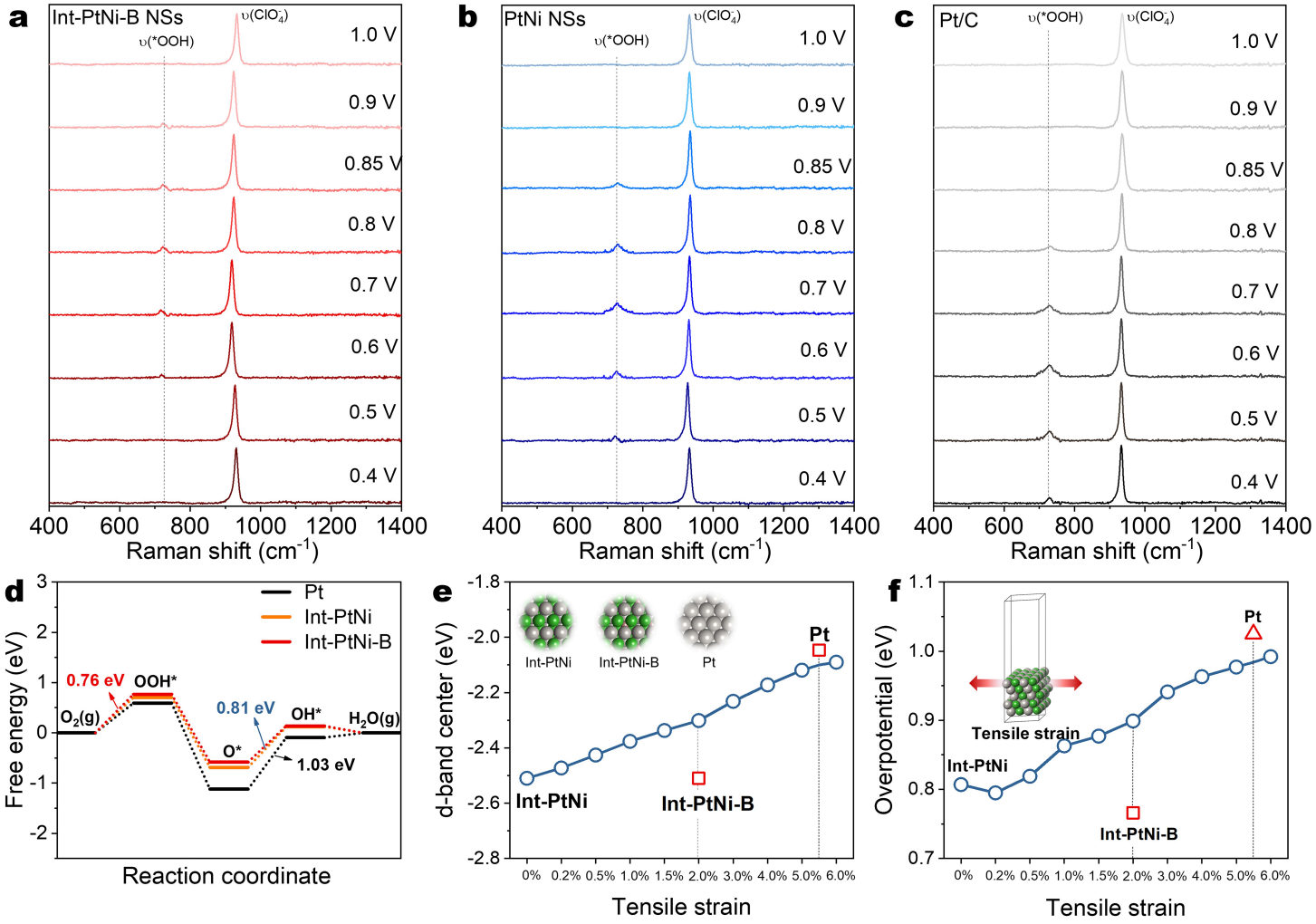


Figure 4

Electronic structure modulation and mechanistic insights into ORR activity. a–c, *In-situ* Raman spectra collected under different applied potentials for Int-PtNi-B NSs (**a**), PtNi NSs (**b**), and Pt/C (**c**), showing the evolution of oxygenated intermediates during the ORR process. **d**, Calculated free energy diagrams of the ORR on Pt, Int-PtNi, and Int-PtNi-B surfaces, highlighting the optimized reaction pathway upon intermetallic ordering and B-incorporation.**e**, Evolution of the d-band center as a function of tensile strain, showing electronic modulation induced by structural and compositional tuning. **f**, Corresponding ORR

overpotential as a function of tensile strain, indicating the interplay between strain and catalytic activity, with Int-PtNi-B deviating from the strain-dominated trend.

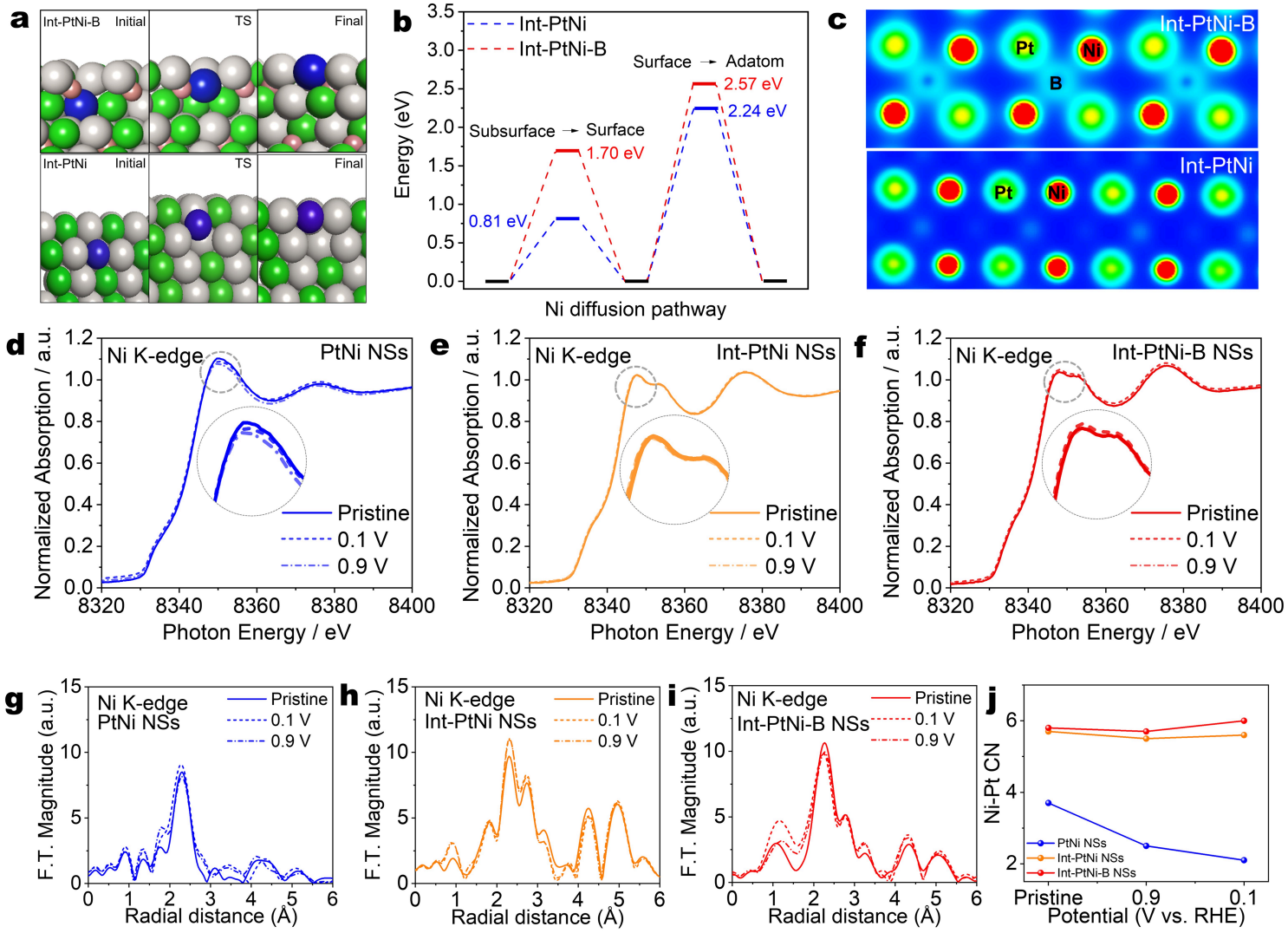


Figure 5

Atomic migration and *in-situ* XAFS analysis of structural stability. a, Schematic configurations and calculated energy profiles for Pt and Ni atomic diffusion pathways on Int-PtNi and Int-PtNi-B surfaces, including initial, transition state (TS), and final states. **b**, Energy barriers for Ni migration along subsurface-to-surface and surface-to-adatom pathways, comparing Int-PtNi and Int-PtNi-B NSs. **c**, Charge density distributions of Int-PtNi-B and Int-PtNi. **d**–**f**, *In-situ* XANES spectra at the Ni K-edge for PtNi NSs (**d**), Int-PtNi NSs (**e**), and Int-PtNi-B NSs (**f**) under different electrochemical potentials. **g**–**i**, Corresponding Fourier-transformed EXAFS spectra at the Ni K-edge, showing the evolution of local coordination environments for PtNi NSs (**g**), Int-PtNi NSs (**h**), and Int-PtNi-B NSs (**i**). **j**, Potential-dependent variation of Ni–Pt coordination numbers, indicating enhanced structural stability of Int-PtNi-B NSs compared to disordered and B-free counterparts.

Supplementary Files

This is a list of supplementary files associated with this preprint. Click to download.

- IntermetallicPtMBNSsSI.docx
- TOC.jpg